Polyhedron 194 (2021) 114931

Contents lists available at ScienceDirect

Polyhedron

journal homepage: www.elsevier.com/locate/poly

Structural, spectroscopic insights, and antimicrobial properties of mononuclear and dinuclear metal(II) carboxylate derivatives with metronidazole

Abiodun A. Ajibola [a,b], Joshua A. Obaleye [a,*], Lesław Sieroń [c], Waldemar Maniukiewicz [c,*], Agnieszka Wojciechowska [d], Andrew Ozarowski [e,*]

[a] Department of Chemistry, University of Ilorin, P.M.B.1515, Ilorin, Kwara State, Nigeria
[b] Department of Chemical Sciences, Crown-Hill University, P.M.B. 1605, Eiyenkorin, Ilorin, Kwara State, Nigeria
[c] Institute of General and Ecological Chemistry, Lodz University of Technology, 90-924 Lodz, Zeromskiego 116, Poland
[d] Faculty of Chemistry, Wroclaw University of Science and Technology, Wyb. Wyspianskiego 27, 50-370 Wroclaw, Poland
[e] National High Magnetic Field Laboratory, Florida State University, 1800 East Paul Dirac Drive, Tallahassee, FL 32310, USA

ARTICLE INFO

Article history:
Received 18 September 2020
Accepted 16 November 2020
Available online 23 November 2020

Keywords:
Metronidazole
DFT
High-Field EPR
X-ray crystal structure
Antimicrobial activity

ABSTRACT

A dinuclear paddle-wheel complex $[Cu_2(PTA)_4(mnz)_2]$ (**1**) and mononuclear $[M(BBA)_2(mnz)_2(H_2O)_2]$ complexes, where PTA = *p*-methylbenzoate, BBA = 2-bromobenzoate, mnz = metronidazole and M = Cu (II) (**2**), Co(II) (**3**), Ni(II) (**4**), Zn(II) (**5**), Cd(II) (**6**) were prepared by adding metronidazole to the mixture of divalent metal nitrate salts and arylcarboxylate acid in alkaline aqueous solution under ambient conditions. The complexes were characterized by elemental analysis, spectroscopy (FTIR, UV–visible and NIR-Vis-UV), single crystal X-ray diffraction (SCXRD), Hirshfeld surface analysis and High-Field EPR. The asymmetry of the $d - d$ bands observed in the electronic diffuse – reflectance spectra of cobalt(II) and nickel(II) complexes is due to the symmetry lowering from O_h to elongated D_{4h} in *trans* – $[MN_2O_2O'_2]$ chromophores. Large zero-field splitting was observed in the HF EPR spectra of the Ni(II) and Co(II) complexes which was modeled by using the CASSCF method. The antimicrobial activity was studied using the agar well diffusion method. The antimicrobial tests of these new compounds were carried out on *Candida albicans* and five bacterial strains (three Gram-negative and two Gram-positive), and were compared to their respective parent ligands. A broad antimicrobial spectrum was observed in some of the complexes.

1. Introduction

Metal(II)-carboxylate complexes have been widely studied over the years due to their vast potential applications in catalysis, biology, pharmacology, magnetism as well as industrial applications [1]. Many of these carboxylate organic ligands can exhibit different modes of coordination when coordinated with metal ions which can be monodentate, bidentate, bridging, chelating-bidentate, bridging-bidentate etc. [2].

Benzoic acid derivatives exhibit different fashion of coordination and sometimes their structure can be influenced by the nature of the auxiliary ligands [3,4]. Carboxyl groups in benzoic acid and most of its derivatives can bridge metal ions and form a variety of multinuclear complexes [5]. In recent times, the use of arylcarboxylic acids and their derivatives in the synthesis of new supramolecular complexes has been explored [6]. There have been many cases where new, diverse and unexpected structures were obtained due to presence of nitrogen and oxygen donor ligands [3,7].

The presence of the hydrophilic and hydrophobic functional groups in the ring of the *p*-methylbenzoic acid (PTA) causes it to act as a surfactant [8]. It has been extensively used in the production of some materials, industrial products and in medicines [9]. Literature survey shows that there are several reports on metal(II) complexes of *p*-methylbenzoic acid and on their applications [10]. In those complexes, PTA acts as a multidentate organic ligand [10].

Halobenzoic acids *e.g.* 2-bromobenzoic acid have been used as reagents in some organic reactions such as the cross coupling reactions [11]. Also, it has served as a building block in the synthesis of nitrogen-containing compounds [12]. Investigations of some transition metal complexes of 2-bromonzoic acid proved that their mode of coordination could be monodentate and chelating [13].

* Corresponding authors.
E-mail addresses: jobaleye@unilorin.edu.ng, jobaleye@yahoo.com (J.A. Obaleye), waldemar.maniukiewicz@p.lodz.pl (W. Maniukiewicz), ozarowsk@magnet.fsu.edu (A. Ozarowski).

https://doi.org/10.1016/j.poly.2020.114931
0277-5387/

Metronidazole [1-(β-hydroxyethyl)-2-methyl-5-nitroimidazole, mnz] also known as Flagyl is an antibiotic drug and a radiosensitizer. This derivative of nitroimidazole has been extensively used and widely studied over many decades due to its pharmaceutical significance [14]. Metronidazole is an approved drug listed by WHO as an essential medicine and as an antimicrobial agent useful in combating various infections [15]. There are many literature reports of successful metronidazole usage in the syntheses of various metal complexes due to its nitrogen atom serving as a donor to the metal ion [16,17]. The presence of the imidazole nitrogen in the structure of metronidazole predicted its monodentate binding mode to a metal ion [16]. However, the usage of metronidazole as a nitrogen donor ligand supporting the carboxylate ligands are limited in literature [18].

In our quest to obtain new compounds, we have synthesized new complexes bearing *p*-methylbenzoic acid (PTA) or 2-bromobenzoic acid (BBA) supported by metronidazole (mnz). These new systems were characterized by spectroscopic methods like FT-IR, UV–Vis, NIR-Vis-UV and high-field electron paramagnetic resonance (HF EPR) spectroscopies. In addition, DFT calculations and Hirshfeld surface analysis of the complexes are presented in this study. The newly synthesized complexes are $[Cu_2(PTA)_4(mnz)_2]$, $[Cu(BBA)_2(mnz)_2(H_2O)_2]$, $[Co(BBA)_2(mnz)_2(H_2O)_2]$, $[Ni(BBA)_2(mnz)_2(H_2O)_2]$, $[Zn(BBA)_2(mnz)_2(H_2O)_2]$ and $[Cd(BBA)_2(mnz)_2(H_2O)_2]$ (Scheme 1).

2. Experimental section

2.1. Materials and instruments

All reagents used in this study were obtained from commercial sources and were used without further purification. Elemental analyses for carbon, hydrogen and nitrogen were performed using a Carlo-Erba analyser (model EA1108). The melting points were determined on MPA100 Optimelt Automated Melting Point System (SRS). The FTIR spectra were recorded over the range 400–4000 cm^{-1} in KBr pellets using a Perkin-Elmer Spectrum Two IR spectrometer (Compound **1**–**6**) and. Fourier transform infrared spectra (FT–IR) were recorded using a Nicolet iS5 FT–IR Spectrometer in the frequency range 4000–400 cm^{-1}) for all parent ligands. The UV–vis spectra of the compound (**1**, **2**, **5** and **6**) were recorded in DMSO using Shimadzu UV-1650PC. The electronic diffuse – reflectance spectra of complexes **3** and **4** were recorded at room temperature on a Cary 500 Scan NIR/Vis/UV spectrophotometer in the range 1500–200 nm, with a resolution of 4 nm. The spectra were enhanced in the *d* – *d* region by using the variable digital method [19] with the following parameters: step = 40 cm^{-1}, α = 300 and N = 30 for cobalt(II) complex (**3**); and step = 30 cm^{-1}, α = 300 and N = 30 for nickel(II) complex (**4**).

2.2. Synthesis.

2.2.1. Synthesis of $[Cu_2(PTA)_4(mnz)_2]$ (**1**)

To the solution of PTA (2 mmol, 0.272 g) in MeOH:H_2O (v/v 10:10), NaOH (2 mmol, 0.08 g) was added, followed by copper nitrate trihydrate (2 mmol, 0.483 g) to form a solution containing a green precipitate after stirring at room temperature for 2 h. Next, metronidazole (mnz) (2 mmol, 0.342 g) was added to the above solution which turned deep green (see eq R1) The deep green solution formed was filtered. The filtrate was allowed to evaporate slowly and after 3 days, green crystals were formed. The crystals were washed and air-dried. See (eq R1) for the step of reaction,

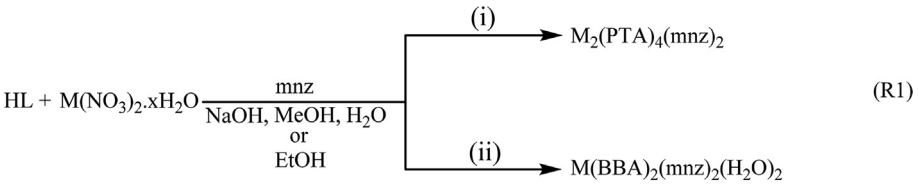

(R1)

For (i)
M = Cu and

x = 3, 4

For (ii)
M = Cu (II), Co (II), Ni (II), Zn (II), Cd (II)

L = PTA or BBA

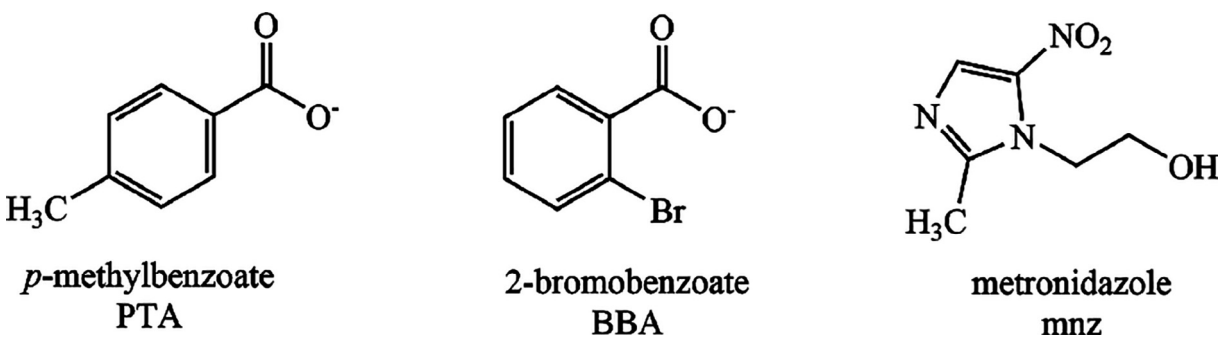

Scheme 1. Structure formulas of ligands used in this study.

Compound 1: Green crystals. Yield. 76%. Melting point: 242 °C. FT IR (KBr cm^{-1}): 3200, 3057, 3031, 1651, 1590, 1539, 1505, 1407, 1373, 1291, 1244, 1211, 1172, 1116, 1037, 1019, 868, 849, 812, 790, 691, 577, 534, 470, 416. Anal. Calc. for $C_{44}H_{52}Cu_2N_6O_{14}$ (%): C, 52.33; H, 4.59; N, 8.32; Found: C, 52.03; H, 4.50; N, 8.40.

2.3. Synthesis of $[Cu(BBA)_2(mnz)_2(H_2O)_2]$ (**2**), $[Co(BBA)_2(mnz)_2(H_2O)_2]$ (**3**), $[Ni(BBA)_2(mnz)_2(H_2O)_2]$ (**4**), $[Zn(BBA)_2(mnz)_2(H_2O)_2]$ (5), $[Cd(BBA)_2(mnz)_2(H_2O)_2]$ (6)

Compounds (**2**)-(**6**) were prepared similarly as (**1**) by using 2 mmol of an appropriate hydrated metal nitrate ($Cu(NO_3)_2{\cdot}3H_2O$ (0.48 g), $Co(NO_3)_2{\cdot}3H_2O$ (0.58 g), $Ni(NO_3)_2{\cdot}3H_2O$ (0.58 g), $Zn(NO_3)_2{\cdot}3H_2O$ (0.60 g) and $Cd(NO_3)_2{\cdot}4H_2O$ (0.62 g)]) and 0.40 g (2 mmol) of 2-bromobenzoic acid in EtOH:H_2O (v/v 10:10).

Compound (**2**): Blue crystals. Yield. 88%. Melting point: 249 °C. FT IR (KBr cm^{-1}): 3144, 1740, 1584, 1549, 1480, 1425, 1388, 1361, 1186, 1150, 1118, 869, 830, 798, 743, 702, 684, 661, 643, 573, 502. Anal. Calc. for $C_{26}H_{30}Br_2CuN_6O_{12}$ (%): C, 37.09; H, 3.59; N, 9.98; Found: C, 37.24; H, 3.47; N, 10.03.

Compound (**3**): Pink crystals. Yield. 82%. Melting point: 244 °C. FT IR (KBr cm^{-1}): 3140, 3029, 1740, 1574, 1543, 1479, 1425, 1399, 1364, 1267, 1231, 1188, 1155, 1119, 1074, 1025, 868, 829, 799, 756, 685, 662, 643, 599, 569, 499, 462, 437, 403. Anal. Calc. for $C_{26}H_{30}Br_2CoN_6O_{12}$ (%): C, 37.30; H, 3.61; N, 10.03; Found: C, 36.94; H, 3.45; N, 9.86.

Compound (**4**): Green crystals. Yield. 89%. Melting point: 203 °C. FT IR (KBr cm^{-1}): 3142, 1573, 1544, 1479, 1426, 1401, 1364, 1268, 1232, 1188, 1156, 1119, 1075, 1044, 1025, 885, 868, 829, 799, 751, 686, 645, 609, 573, 499, 463, 439. Anal. Calc. for $C_{26}H_{30}Br_2NiN_6O_{12}$ (%): C, 37.31; H, 3.61; N, 10.04; Found: C, 36.90; H, 3.52; N, 9.69.

Compound (**5**): Colorless crystals. Yield. 85%. Melting point: 248 °C. FT IR (KBr cm^{-1}): 3138, 3029, 1740, 1574, 1543, 1478, 1426, 1386, 1364, 1267, 1231, 1188, 1154, 1120, 1074, 1024, 868, 828, 799, 744, 684, 643, 598, 568, 499, 460, 434, 403. Anal. Calc. for $C_{26}H_{30}Br_2ZnN_6O_{12}$ (%): C, 37.01; H, 3.58; N, 9.96; Found: C, 37.14; H, 3.44; N, 10.03.

Compound (**6**): Colorless crystals. Yield. 87%. Melting point: 242 °C. FT IR (KBr cm^{-1}): 3132, 1740, 1574, 1542, 1478, 1426, 1397, 1363, 1267, 1230, 1189, 1155, 1074, 1025, 868, 828, 798, 744, 682, 643, 618, 584, 565, 502, 459, 431. Anal. Calc. for $C_{26}H_{30}Br_2CdN_6O_{12}$ (%): C, 35.06; H, 3.39; N, 9.43; Found: C, 34.92; H, 3.38; N, 9.29

2.4. X-ray crystallography

Single crystal diffraction data were collected by the ω-scan technique using CuKα (λ = 1.54184 Å) for (**1**)-(**3**) and MoKα (λ = 0.71073 Å) for (**4**)**-(6)** radiation, respectively. The crystals (**1**)**-(6)** were studied at 100 K using a RIGAKU XtaLAB Synergy, Dualflex, Pilatus 300 K diffractometer [20] with Photon Jet microfocus X-ray Source Data collection, cell refinement, data reduction and absorption correction were carried out using CrysAlis PRO software [20]. The crystal structures were solved by using direct methods with the SHELXT 2018/2 program [21]. Atomic scattering factors were taken from the International Tables for X-ray Crystallography. Positional parameters of non-H-atoms were refined by a full-matrix least-squares method on F^2 with anisotropic thermal parameters by using the SHELXL 2018/3 program [22]. All hydrogen atoms were located in the difference electron density map. Hydrogen atoms bonded to carbon were placed in calculated positions (C—H = 0.93–0.98 Å) and included as riding contributions with isotropic displacement parameters set to 1.2 times the U_{eq} of the parent atom. In the case of water molecules, H atoms were treated with O—H = 0.86 Å and were refined without any restraints. Molecular graphics were prepared by using Mercury program [23]. Crystal data and structure refinement parameters are shown in Tables S1 and S2, while selected geometric parameters are collected in Table S3.

2.5. Hirshfeld surface analysis

The Hirshfeld surfaces [24] and the related 2D-fingerprint plots [25] were calculated using a Crystal Explorer program [26]. The CIF file of each structure was imported into the program and a high resolution Hirshfeld surfaces were mapped with the function d_{norm}. Before starting the calculation the bond lengths to hydrogen atoms were set to standardized neutron values (O—H = 0.983 Å, N—H = 1.009 Å and C—H = 1.083 Å). Then, the HF surfaces were resolved into 2D-fingerprint plots, in order to quantitatively determine the nature and type of all intermolecular contacts experienced by the molecules in the crystal. These plots were produced using the standard 0.6–2.6 Å view with the d_e and d_i distance scales displayed on the graph axes.

2.6. DFT studies

The theoretical exchange coupling constants were obtained using a broken symmetry approach [27], as implemented in the program ORCA [28]. Functional B3LYP was employed. The exchange integral was determined from the difference of the SCF energies predicted for the S = 1 and the broken-symmetry (S = 0) state. The BS state corresponds to configurations for which one spin-up electron is localized on one site and one spin-down electron on the other site. The *J* values corresponding to the Hamiltonian H = JS_1S_2 were evaluated using the expression $J = 2(\varepsilon_F - \varepsilon_{BS})/\left(\left\langle \widehat{\mathbf{S}}^2 \right\rangle_{HF} - \left\langle \widehat{\mathbf{S}}^2 \right\rangle_{BS}\right)$, where $\varepsilon$are the energies and $\left\langle \widehat{\mathbf{S}}^2 \right\rangle$are the average values of the total spin-squared operator of the ferromagnetic and BS states. A calculation of the spin Hamiltonian parameter *D* was also attempted for the Ni and Co complexes, using the X-Ray structure and the CASSCF method [29–31].

2.7. High field EPR

High-frequency EPR spectra were recorded on a home-built spectrometer at the EMR facility of NHMFL. The instrument is a transmission-type device in which waves are propagated in cylindrical light-pipes. The microwaves were generated by a phase-locked oscillator (Virginia Diodes) operating at a frequency of 8–20 GHz and generating its harmonics, of which the 4th, 8th, 12th, 16th, 24th, 32nd and 48th were available. A superconducting magnet (Oxford Instruments) capable of reaching a field of 17 T was employed.

2.8. Antimicrobial screening

Agar well diffusion method [32] was used for the *in vitro* study of five bacteria strains including *Candida albicans.* The five clinical isolates and one fungus organism used for the antimicrobial investigation namely; three Gram-negative bacteria *Escherichia coli, Salmonella typhi, Klebsiella pneumonia,* two Gram-positive bacteria *Micrococcus luteus, Staphylococcus aureus*, and *C. albicans* were kindly donated by the Department of Microbiology Laboratory, University of Ilorin, Ilorin, Nigeria. Nutrient agar was used in purification of isolates. Isolates were then suspended into a sterile phosphate buffered saline and standardized using 0.5 McFarland standard. Mueller Hinton Agar was used for the susceptibility. The agar was poured aseptically, allow to solidify and dry for 15 mins. Standardized isolates suspension was inoculated into the agar using swab stick. The Cork borer of 10 mm was used on mak-

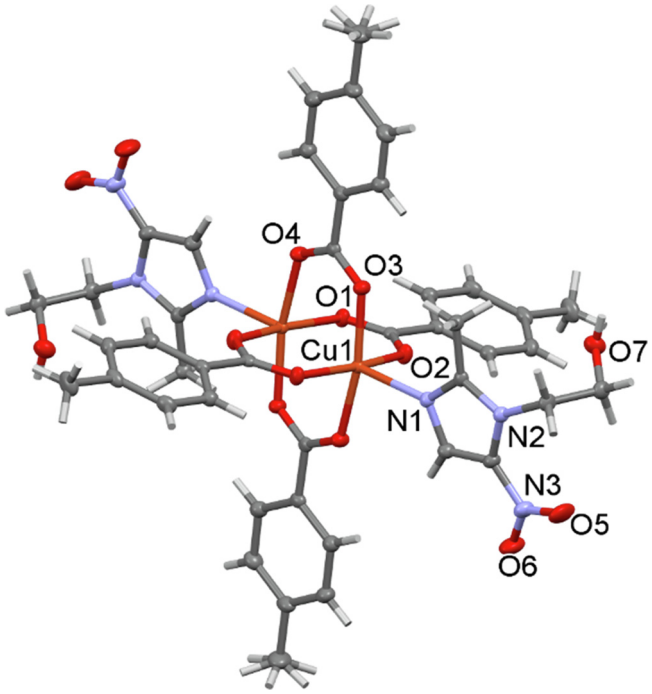

Fig. 1. Perspective view of (**1**), with the selected atom numbering scheme. Thermal ellipsoids are drawn at the 50% probability level.

ing well into the solidified agar. Then 50 µL of the sample (12 mg/2 ml) was introduced into the well and allow to diffuse. Plate was incubated for 24 h at 37 °C and zone of clearance was observed and were carefully measured appropriately.

The experiments were duplicated, measured in millimeters and the average value were recorded. Commercially available DMSO was used as a solvent in dissolving the samples. The solvent used also served as the control for the antibacterial test.

3. Results and discussion

3.1. Crystal structures

The compound (**1**), $[Cu_2(PTA)_4(mnz)_2]$, crystallizes in a triclinic crystal system with a space group P-1. The structure consists of centrosymmetric dinuclear molecules with paddle-wheel cage (Fig. 1), which is quite common in Cu(II) carboxylates [33]. Based on a review of similar structures in the Cambridge Crystallographic Data Base, in the paddle-wheel molecules CuO_4N type, the Cu···Cu distance varies between 2.575 and 3.261 Å with a mean value of 2.675 Å [34]. In compound (**1**) the Cu···Cu distance is 2.677(1) Å. Each Cu(II) ion is coordinated by N atom from a metronidazole [Cu1-N1 = 2.1854(15)Å] and four O atoms from two *p*-methylbenzoate ligands [mean bond lengths Cu–O = 1.9728(13)Å] forming a slightly distorted square pyramidal geometry. The Cu atom is moved from the plane of four oxygen atoms in the direction of nitrogen by 0.2192(3)Å. The deformation of the Cu coordination sphere from idealized square-pyramidal geometry toward the trigonal bipyramid can be characterized by parameter τ defined by Addison *et al.* [35], (τ = 0.005; cf. the τ values for the idealized geometries are τ = 0, square planar, τ = 1, trigonal bipyramidal). The equatorial Cu–O bonds are shorter than the axial Cu–N bonds due to the Jahn-Teller effect. They are comparable to similar paddle-wheel structures described in the literature [36].

Fig. 2 shows the packing of the molecules (**1**) in the crystal. The structure is stabilized by weak interaction of type C—H···O (Table S4). It shows the characteristic interaction of p-methylbenzoate rings in the crystal.

All mononuclear $[M(BBA)_2(mnz)_2(H_2O)_2$, where M = Cu, Co, Ni, Zn, Cd] complexes are isostructural with the M atom lying on an inversion center. They crystallize in the monoclinic system with the space group $P2_1/n$. The perspective views of the crystal structure of complexes (**2**)–(**6**) are shown in Fig. 3 and Figs. S1–4 respectively, and their selected geometric parameters are given in Table S3**.** The structures consist of *trans*-centrosymmetric molecules in which the central M atoms are six-coordinated. The coordination sphere consists of two 2-bromobenzoate, two metronidazole ligands and two coordinated water molecules, all ligands being monodentate. The coordination polyhedron can be described as a slightly distorted tetragonal bipyramid. Two equatorial positions are occupied by two nitrogen atoms of the metronidazole ligands [M1–N1 bond lengths vary form 2.0216(17) Å to 2.3201(15) Å], while the other two equatorial positions are occupied by oxygen atoms [M1–O5 bond lengths vary form 1.9993 (14) Å to 2.2944(12) Å] of carboxyl groups of two 2-bromobenzoate anions. The axial positions are occupied by water molecules at longer bond distances. The [M1–O1 bond lengths vary form 2.0704(12) Å to 2.3743(17) Å].

The 3D supramolecular packing of (**2**)-**(6)** is regulated by O—H···O, and C—H···O hydrogen-bonding interactions (Table S4). The water molecules, which are coordinated to M atoms, are

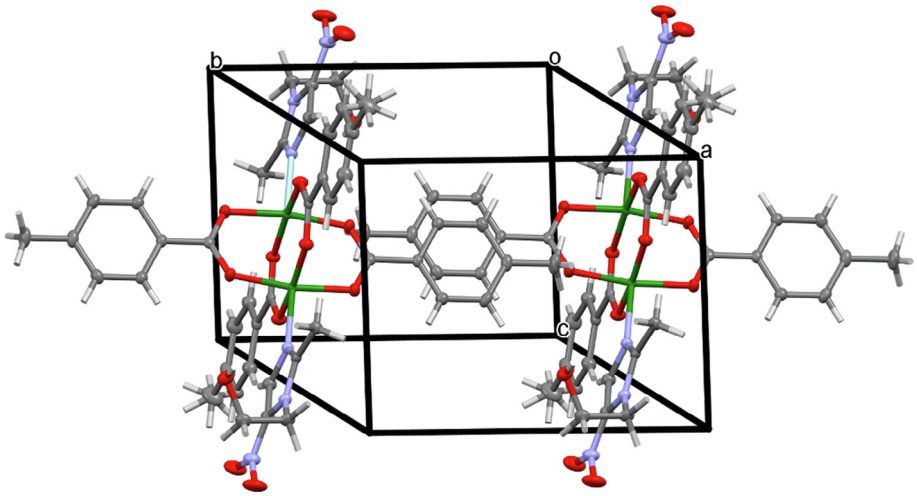

Fig. 2. Packing diagram of complex (**1**).

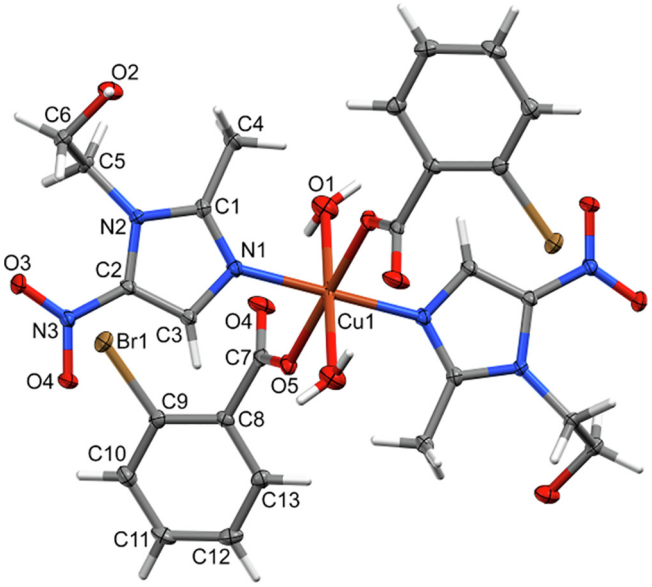

Fig. 3. Ortep diagram of $Cu(BBA)_2(mnz)_2(H_2O)_2$ (**2**). The ellipsoids are drawn at 50% probability level.

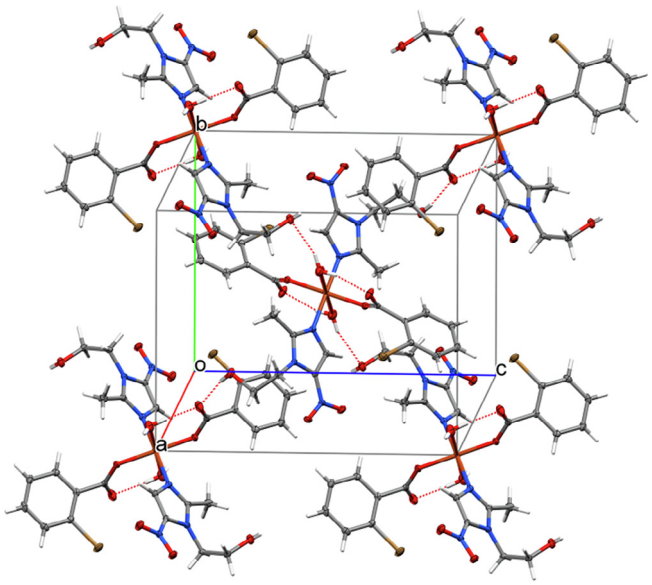

Fig. 4. Packing diagram of (**2**) showing intra- and intermolecular O—H···O hydrogen bonds.

involved in the formation of intra- and intermolecular hydrogen bonds **(**Fig. 4**).**

3.2. Hirshfeld surface analysis

The intermolecular interactions of crystal structures (**1**)–(**6**) were quantified using Hirshfeld surface analysis [24] and fingerprint plots (FP) [25]. Fig. 5 illustrates samples of Hirshfeld surfaces for structures (**1**) and (**2**) respectively. The dominant intermolecular interactions C—H···O for (**1**) and O—H···O for (**2**)-**(6)** are viewed by the bright red area of the d_{norm} surface. In general, the Hirshfeld surface analysis suggests that the crystal packing in structures (**1**)-**(6)** is largely dominated by the common planar components of ligands, leading to close H···H intercontacts. However, in (**2**)-**(6)** structures, the predominance of the O—H···O interactions is also evident (Fig. 5)

Fig. 6 illustrates the two-dimensional fingerprint plots of the HS for structures (**1**) and (**2**)**.** The fingerprint plots for the remaining structures (**3**)-**(6)** are shown in Fig. S6. The quantitative comparison of intercontacts for all structures and the relevant intermolecular interactions are presented in Table S5**.** The majority of the contacts are H···H interactions, with the proportion of these varying from *ca.* 30.5% [for (**2**)-**(6)]** to 44.8% [for (**1**)]. Noticeably, there is a higher proportion of H···H contacts on the HS surface of (**1**) compared to the rest of complexes. This is due to the greater overlap of p-methylbenzoate rings in the structure (see Fig. 2). The 2D fingerprint plots of (**2**)-**(6)** consistently showed the greatest percentages for the H···O/O···H contacts, accounting for ca 30%. Apparently, the variation is in the other nonbonding interactions. The next strong interactions in (**2**)-**(6)** are the H···C/C···H and H···Br/Br···H, which contribute ca 16% and ca 12% respectively.

3.3. FT-IR spectroscopy

Relevant absorption bands in infrared spectra of compounds 1–6 are shown in Fig. S7 which also includes the parent ligands (metronidazole, mnz, Paratoluic acid, PTA, and 2-bromobenzoic acid, BBA). A band at 1534 cm^{-1} in the IR spectrum of metronidazole (mnz), is attributed to υ_{as}(C═N). Upon complexation this particular band shifted to higher frequencies in all compounds 1–6 and was observed between 1540 and 1563 cm^{-1} [16]. This is due to the coordination of the N3 atom of the imidazole ring to each metal ions. Also, both the alcoholic group ($_{as}$(C—O)) in the metronidazole remains in the same region as in the complexes synthesized. In the case of υ(C—O)$_{alcoholic\ group}$, the bands appear at 1175 cm^{-1} (compound 1), and between 1186 and 1189 cm^{-1} for compounds 2–6 respectively.

Other groups present in the complexes are $–NO_2$ and –COO-. The splitting of bands for $–NO_2$ and –COO- group corresponds to asymmetric and symmetric vibrations in the complexes. The υ_{as}($-NO_2–$) and $\upsilon_s(NO_2–)$ bands appears at 1475 and 1370 cm^{-1}, respectively in **1**, while in **2**–**6** they are observed at 1480 and 1365 cm^{-1}, respectively. The frequency difference $\Delta\upsilon_{NO2}$- = $\upsilon_{as}(NO_2–)$ - υ_s($-NO_2–$) ranges from 105 cm^{-1} for **1** to 115 cm^{-1} for **2**–**6** compared to 105 cm^{-1} in free metronidazole, showing that the $NO_2–$ group is not taking part in the coordination in **1**–**6**. Also, for –COO- groups, the bands $\upsilon_{as}(CO_2–)$ and $\upsilon_s(CO_2–)$ appear at 1610 and 1400 cm^{-1}, respectively in **1**, while their positions in other compounds are 1580 and 1390 cm^{-1} in **2**, 1575 and 1400 cm^{-1} in compounds **3**–**5**, 1575 and 1395 cm^{-1} in **6**. The rocking (ρr) mode of coordinated H_2O molecules ($M–H_2O$) in all compounds except for **1** showed strong bands at 828–830 cm^{-1}. Finally, the bands at 511/448 cm^{-1} (**1**), 574/444 cm^{-1} (**2**), 570/438 cm^{-1} (**3**), 573/440 cm^{-1} (**4**), 569/435 cm^{-1} (**5**), 565/431 cm^{-1} (**6**) may be attributed to M–O/M–N stretching vibrations.

3.4. Electronic spectroscopy NIR – Vis – UV

The UV–Visible spectra of **1**, **2**, **5** and **6** were recorded in DMSO. In the spectra of **1** and **2**, bands are observed in the visible region at 759 nm (ε_{max} = 115 $L.mol^{-1}.cm^{-1}$) (**1**) and 729 nm (ε_{max} = 202 $L.mol^{-1}.cm^{-1}$) (**2**). These single-electronic *d-d* absorptions bands, which are observed in copper(II) ion in pseudo – octahedral crystal field, were attributed to the spin – allowed $^2E_g \rightarrow {}^2T_{2g}$ transition (Fig. 7).

Zinc(II) (**5**) and cadmium(II) (**6**) complexes possess completely filled *d* orbitals (d^{10} configuration) and therefore lack the *d* – *d* bands. Thus, the electronic spectra present bands only at wavelength below 400 nm (where **5** is observed at 283 nm, ε_{max} = 1422 $L.mol^{-1}.cm^{-1}$ and **6** at 283 nm, ε_{max} = 1608 $L.mol^{-1}.cm^{-1}$) which are assigned to the high intensity dipole – allowed electronic intraligand $\pi \rightarrow \pi^*$ transition in the ring excitation in the

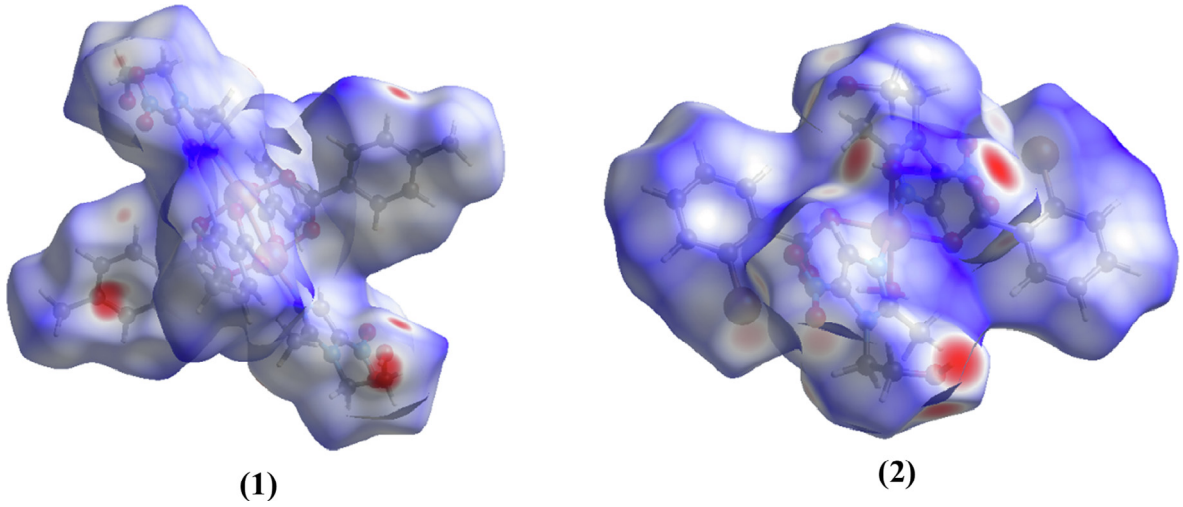

Fig. 5. Views of the Hirshfeld surfaces for (**1**) and (**2**) mapped with d_{norm}.

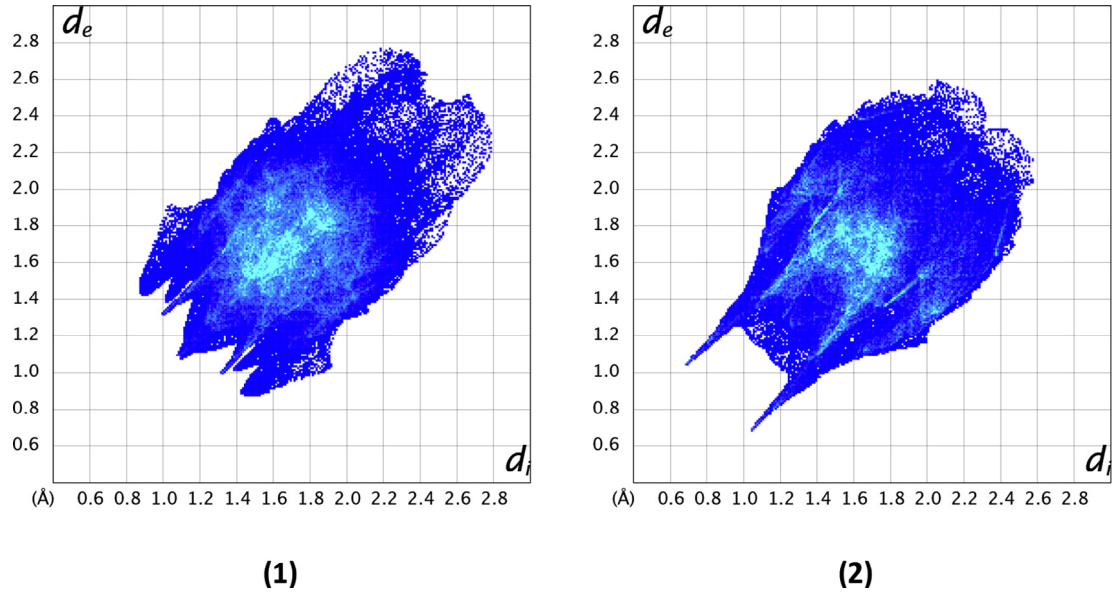

Fig. 6. Fingerprints of the compounds (**1**) and (**2**)

metronidazole and 2-bromobenzoate (Fig. S8). These transitions generate also bands at 360 nm, 312 nm and 247 nm in spectra of solid sample of cobalt(II) and nickel(II) complexes, **3** and **4**, respectively (Fig. S9).

The electronic diffuse – reflectance spectra of complexes **3** and **4** are shown in Fig. 8. In the range 1400–400 nm, spectra exhibit low-intensity bands characteristic for spin-allowed and spin-forbidden $d - d$ transitions for high-spin six-coordinated Co(II) (d^7 configuration) and Ni(II) (d^8 configuration) ions (Fig. 8 and S9). The asymmetry of the $d - d$ bands implies splittings due to crystal field symmetry lower than O_h. The donor nitrogen and oxygen atoms form the *trans* – $[MN_2O_2O'_2]$ chromophore (M = Co(II), Ni (II)) of pseudo – octahedral geometry elongated along the N16 – Co1 – N16 and N15 – Ni1 – N15 bonds, in **3** and **4**, respectively.

The spectrum of cobalt(II) complex presents a distinguished band with maximum at 1150 nm and a wide absorption from 650 nm to 430 nm with double maximum at 495 nm and 470 nm. Assuming the O_h symmetry, these bands are generated by the $^4T_{1g}(^4F) \rightarrow {}^4T_{2g}(^4F)$ (ν_1), $^4T_{1g} \rightarrow {}^4A_{2g}(^4F)$ (ν_2) and $^4T_{1g}(^4F) \rightarrow {}^4T_{1g}(^4P)$ (ν_3) transitions, respectively (Fig. 9) [37–39]. The tetragonally elongated crystal field (D_{4h}) removes degeneration of the $^4T_{1g}(^4F)$, $^4T_{2g}(^4F)$ and $^4T_{1g}$ (^4P) terms to produce pairs of $^4E_g(1)$ + $^4A_{2g}$, $^4B_{2g}$ + $^4E_g(2)$ and $^4A_{2g}$ + ^4E_g (**3**) levels. The ^4E_g ($^4T_{1g}(^4F)$, O_h) term is a ground state in the elongated geometry [40]. The $^4A_{2g}(^4F)$ state becomes the $^4B_{1g}$ level. The filtering process of the spectrum has revealed no splitting of the band at 1150 nm into two components, probbably due to a very small difference in energy values of $^4E_g(1) \rightarrow {}^4B_{2g}$ ($^4T_{2g}(^4F)$, O_h) and $^4E_g(1) \rightarrow {}^4E_g(2)$ ($^4T_{2g}(^4F)$, O_h) transitions (Fig. S10a). Thus, this band arises from both transitions. The band assigned as $^4E_g(1) \rightarrow {}^4B_{1g}$ ($^4A_{2g}(^4F)$, O_h) transition is usually very weak and difficult to observe. Under the filtration process, a weak feature at *ca.* 615 nm is clearly seen and can be assigned to the $^4E_g(1) \rightarrow {}^4B_{1g}$ transition (Fig. S10a). The spin – allowed quartet – quartet $^4E_g(1) \rightarrow {}^4A_{2g}$ ($^4T_{1g}(^4P)$, O_h) and $^4E_g(1) \rightarrow {}^4E_g(3)$ ($^4T_{1g}(^4P)$, O_h) transitions undoubtedly generate the bands with maxima at 495 nm and 470 nm (Fig. 8).

In the spectrum of nickel(II) complex **4**, the first and second $d - d$ bands with maxima *ca.* 1100 nm and 630 nm are asymmetric implying a splitting of each band (Fig. 8). The third band expected

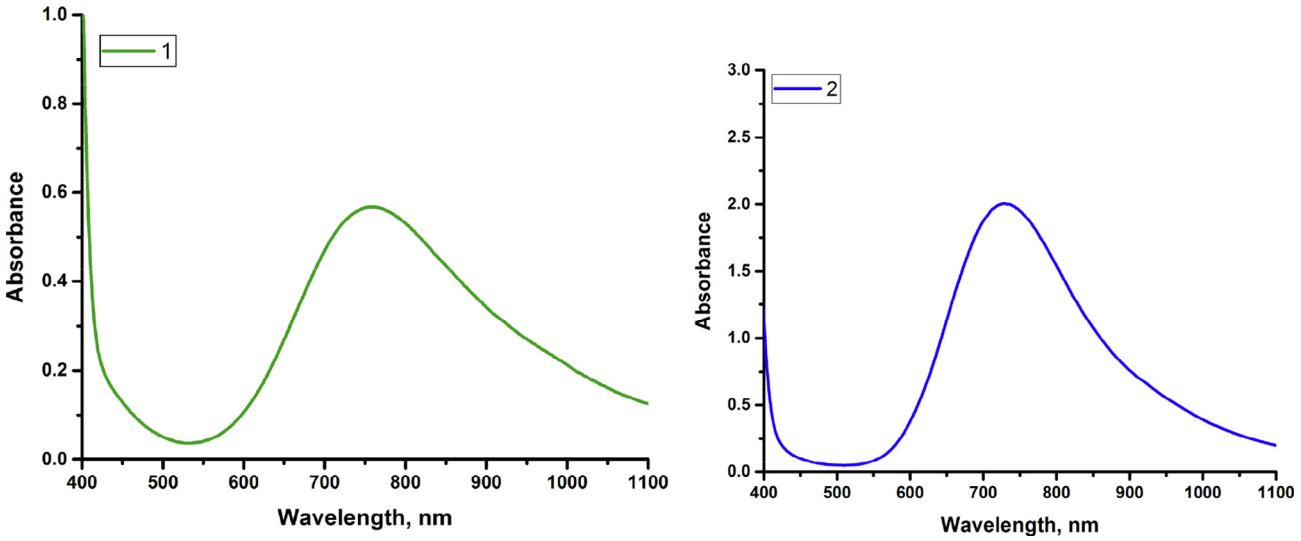

Fig. 7. UV–Visible spectra of **1** and **2** recorded in DMSO.

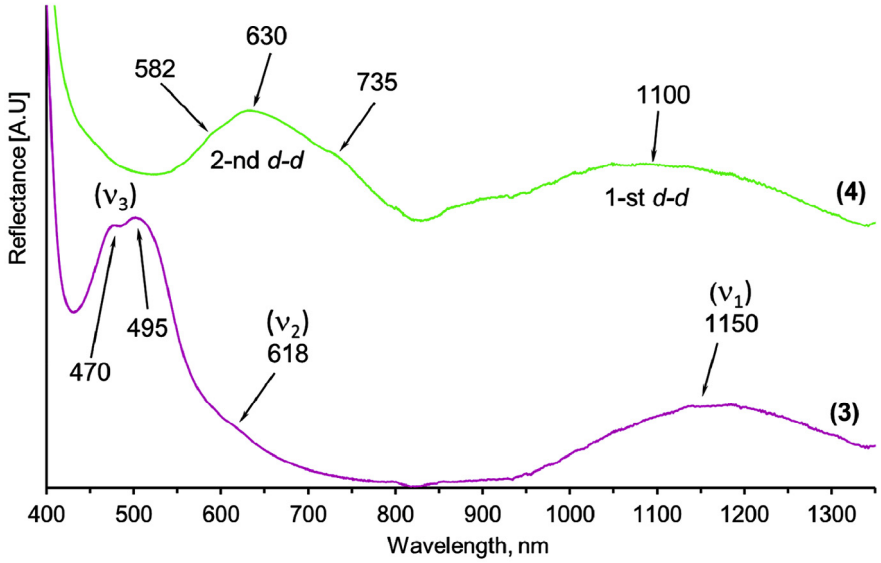

Fig. 8. The $d - d$ spectral range of NIR-Vis-UV diffuse-reflectance electronic spectra at room-temperature of cobalt(II) and nickel(II) complexes, **3** and **4**.

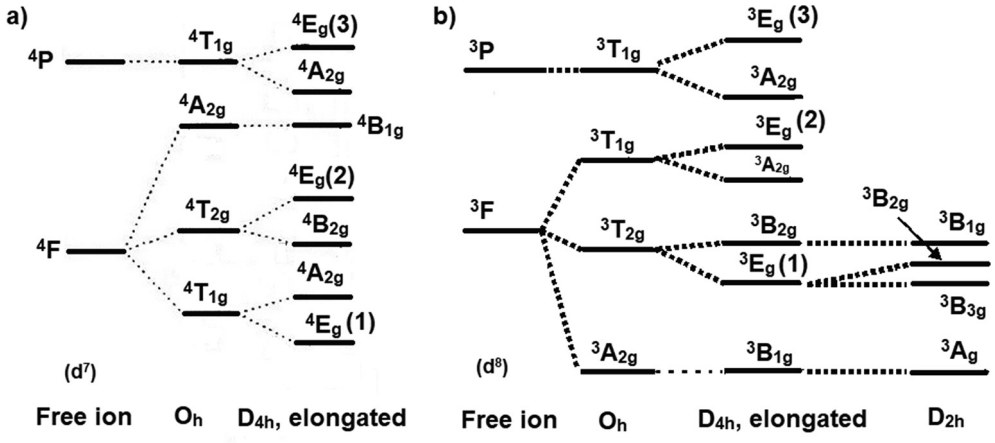

Fig. 9. Term diagram of a) the Co(II) and b) the Ni(II) ions in various coordination environments [37,38,39,40,41].

at *ca.* 390 nm is masked by unresolved absorptions due to charge – transfer (CT) transitions. Symmetry lowering from octahedral to elongated D_{4h} transforms the ground term $^3A_{2g}(^3F, O_h)$ into $^3B_{1g}$ (Fig. 9) [37,40f,41]. Two spin – triplet states $^3T_{2g}(^3F, O_h)$ and $^3T_{1g}$ (^3F, O_h) are split into pairs of levels: $^3E_g(1)$ + $^3B_{2g}$ and $^3A_{2g}$ + $^3E_g(2)$. The components of the 1-st *d-d* band in the electronic spectra are due to the spin – allowed $^3B_{1g} \rightarrow {}^3E_g(1)$ and $^3B_{1g} \rightarrow {}^3B_{2g}$ transitions at *ca.* 1180 nm and 1060 nm (filtering analysis, Fig. S10b). The wavelengths obtained for $^3B_{1g} \rightarrow {}^3E_g(2)$ and $^3B_{1g} \rightarrow {}^3A_{2g}$ transitions (2 – nd *d-d*) equal 636 nm and 585 nm, respectively. It is noteworthy that the 2-nd *d* – *d* band show a sharp feature at 740 nm ascribed to "intensity borrowing" from the first spin forbidden $^3B_{1g} \rightarrow {}^1A_{1g} + {}^1B_{1g}$ (^1E_g, O_h) transitions as in the case [Ni$(H_2O)_4$(1-mhyd)$_2$] (1-mhyd = 1-methylhydantoin) [42] or [Ni(2-MeSnic)$_2$(iq)$_2$$(H_2O)_2$] (2-MeSnic = 2-methylsulfanylnicotinato, iq = *iso* – quinoline) [43]. The subsequent spin-forbidden $^3B_{1g} \rightarrow {}^1B_{2g} + {}^1E_g$ ($^1T_{2g}(^1D)$, O_h), $^3B_{1g} \rightarrow {}^1A_{1g}$ ($^1A_{1g}(G)$,O_h) and $^3B_{1g} \rightarrow {}^1E_g + {}^1A_{2g}$ ($^1T_{1g}(^1G)$, O_h) transitions can generate very low intensity bands usually observed between the second and third *d* – *d* band. From the spectra filtration it was possible to find only two such bands at 508 nm and 461 nm with no evidence of splitting. Thus, the weak absorption over the range 800 nm to 450 nm correspond to the $^3B_{1g} \rightarrow {}^1B_{2g} + {}^1E_g$ ($^1T_{2g}(^1D)$ and $^3B_{1g} \rightarrow {}^1A_{1g}$ ($^1A_{1g}(G)$ transitions. Finally, the $^3B_{1g} \rightarrow {}^1E_g + {}^1A_{2g}$ ($^1T_{1g}(^1G)$, O_h) band is obscured by the high intensity CT bands.

3.5. High field EPR

3.5.1. Binuclear complex 1

Copper "paddlewheel" carboxylates are typically strong antiferromagnets with the exchange integral *J*, corresponding to the Heisenberg Hamiltonian in a form H = JS_1S_2, of about 300 cm^{-1} [33]. In such systems, the diamagnetic singlet (S = 0) is the ground state, while the excited triplet state (S = 1) has energy equal to *J* [33]. Accordingly, the magnetic susceptibility approaches 0 at low temperatures and rises with increasing temperature, reaching (with J = 300 cm^{-1}) just ~ 395·10^{-6} cm^3/mol (per 1 Cu atom) at 300 K, which corresponds to the effective magnetic moment of 0.97 B.M. For comparison, a susceptibility of ~ 1420·10^{-6} cm^3/mol and magnetic moment of 1.84 B.M. is expected for a monomeric Cu^{2+} complex at 300 K. The magnetic properties of the copper "paddlewheel" dimers exhibit little variety and the magnetic susceptibility of **1** was not measured in this work. The EPR spectra are due to transitions within the excited spin-triplet state, and they

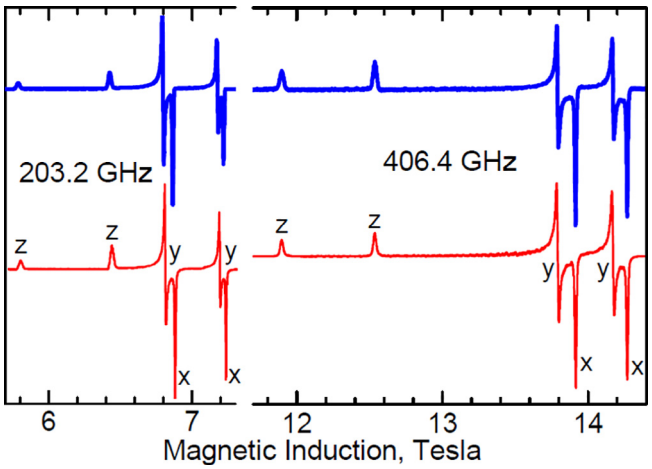

Fig. 10. High-Field EPR spectra of the binuclear complex **1** recorded at 150 K with microwave frequencies as indicated. Top: experimental; bottom: simulated. Labels x, y and z indicate the molecular orientations at which respective transitions occur.

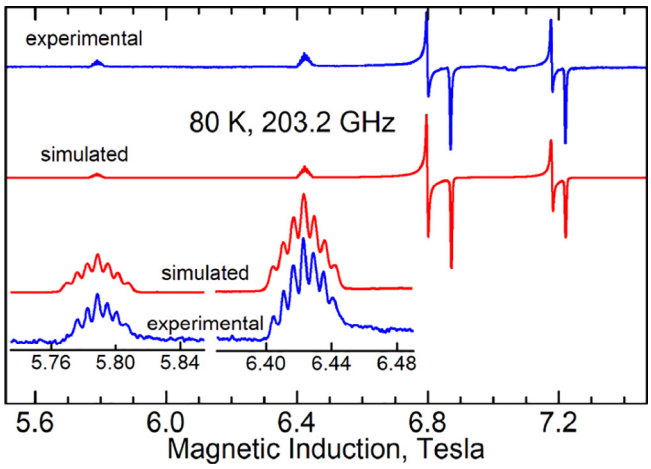

Fig. 11. Experimental and simulated HF EPR spectra of **1**. The insets show the "parallel" features of the spectrum with resolved hyperfine structure due to two copper nuclei (nuclear spin I_{Cu} = 3/2).

vanish at low temperatures when the triplet state becomes depopulated. The binuclear copper compound **1** exhibited HF EPR spectra characteristic for the "paddlewheel" complexes. It produced high-quality HF EPR spectra at room temperature, at 150 K (Fig. 10) and at 80 K (Fig. 11), while spectra at 50 K were not usable. EPR spectra of triplet states are described in terms of the standard spin Hamiltonian

$$\widehat{\boldsymbol{H}} = \mu_B \boldsymbol{B}\{\boldsymbol{g}\}\widehat{\boldsymbol{S}} + D\left\{\widehat{\boldsymbol{S}}_z^2 - \frac{1}{3}S(S+1)\right\} + E\left(\widehat{\boldsymbol{S}}_x^2 - \widehat{\boldsymbol{S}}_y^2\right) \quad (1)$$

For **1**, g_x = 2.059(2), g_y = 2.076(2), g_z = 2.377(1), *D* = −0.354(1) cm^{-1}, *E* = −0.0056(4) cm^{-1}. The sign of *D* could not be determined from the powder spectra obtained in this work, but it has been found to be negative in the copper "paddlewheels" by single-crystal HF EPR studies [44], and confirmed by theoretical calculations [45]. For comparison, the spin Hamiltonian parameters for copper acetate monohydrate are g_x = 2.054, g_y = 2.079, g_z = 2.364, *D* = −0.335 cm^{-1}, *E* = −0.0103 cm^{-1} [44].

Hyperfine structure due to two copper nuclei (nuclear spin I = 3/2) was observed at 150 K and particularly well at 80 K, where the resonances became narrower thanks to the fact that most of the dimer molecules are at 80 K in diamagnetic ground state with S = 0, and the molecules still remaining paramagnetic are diluted by the diamagnetic ones. The hyperfine structure consists of 7 resonances with relative intensities 1:2:3:4:3:2:1 and separated by *ca.* 60 Gauss (Fig. 11).

The g values in copper(II) complexes with the d_x2-$_y2$ ground state are related to the crystal field splitting of the d orbitals:

$$g_z = 2.0023 - \frac{8\lambda}{\Delta E_{x^2-y^2\,xy}}$$
$$g_{x(y)} = 2.0023 - \frac{2\lambda}{\Delta E_{x^2-y^2\,yz(xz)}} \quad (2)$$

Only one unresolved band centered at 13200 cm^{-1} is observed in **1**. With the spin–orbit coupling constant for Cu^{2+}, λ = −828 cm^{-1}, $g_{x(y)}$ and g_z of 2.127 and 2.504, respectively would be expected. The significantly smaller experimental values, g_z = 2.377 and the average of g_x and g_y of 2.067 are due to the unpaired electron delocalization onto the ligands. Formulas above indicate that λ is reduced to 75% and 52% of its free-ion magnitude, at the z and x,y orientations, respectively. The DFT calculations indicate an unpaired electron density on the copper ion of 67% in a rough agreement with the above numbers. The zero-field parameters in **1** are not surprising. The *D* parameter in simple copper "paddlewheels" tends to be around −0.33 cm^{-1} and around −0.43 cm^{-1} in complexes of

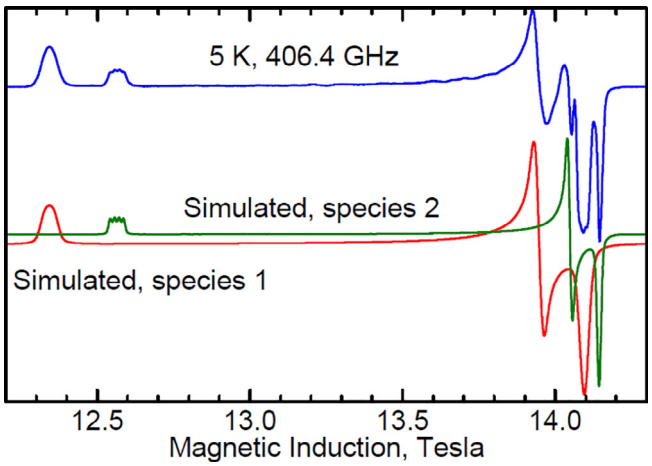

Fig. 12. HF EPR spectra of **2**. Blue: experimental; red: simulated with g_x = 2.060, g_y = 2.082, g_z = 2.352. Green: simulated with g_x = 2.053, g_y = 2.067, g_z = 2.311, A_z = 0.0167 cm^{-1}. ((Colour online.))

halogenated aliphatic carboxylic acids [33,44], and in some other carboxylate dimers like [Cu_2(1,8-naphthalimido)-ethanoate)$_4$(-bipy)] [46].

3.5.2. Complex 2

Unexpectedly, spectra of complex **2** reveal presence of two species in comparable amounts (Fig. 12). The g_z parameter of the first species is surprisingly high for a copper complex with two nitrogen atoms in the xy plane. Parameters of species 2 fit the molecular structure better. The relationship between the g_z values of the two species suggests that species 1 has less nitrogen atoms in the xy plane than species 2. Possibly, one mnz molecule was substituted by water. Apparently, this is a case where a crystal is not fully representative of a bulk sample. Finally, it should be noted here that these two species would not be resolved in X-Band EPR – the distance between the Z features at 406 GHz is 2200 Gauss but only ~ 55 Gauss at the X-Band frequency of 9.5 GHz, which is much less than linewidth in species 1 or the hyperfine splitting in species 2.

3.5.3. Cobalt and nickel complexes

The nickel complex **4** exhibited nicely resolved spin-triplet state spectra (Fig. 13) which could be interpreted in terms of spin Hamiltonian (**1**). The HFEPR spectra were recorded at many microwave frequencies and the frequency dependencies of the resonance fields (Fig. 14) were fitted to obtain g_x = 2.205(2), g_y = 2.200(2), g_z = 2.224(2), D = −3.508(6) cm^{-1}, E = −0.598(4) cm^{-1} (E/D = 0.17). It should be emphasized here that the sign of D is easily determined if the powder HFEPR spectra can be recorded at sufficiently low temperature, which is the case here.

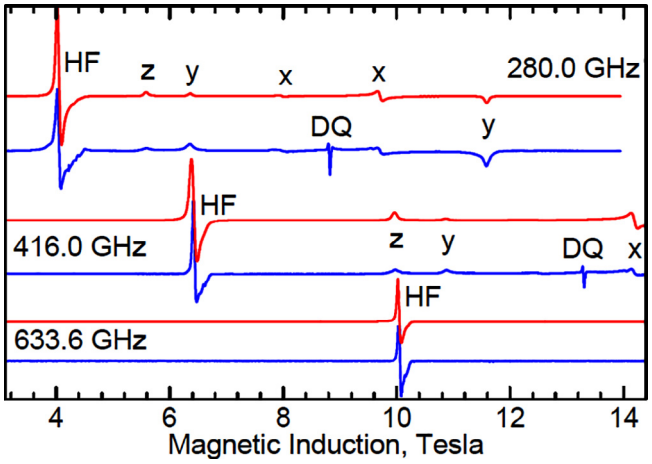

Fig. 13. HF EPR spectra of the nickel complex **4** recorded at 5 K. Blue: experimental; red: simulated. Labels x, y and z indicate the molecular orientations at which respective transitions occur. HF: half-field transition (ΔM_S = 2); DQ: double-quantum transition. ((Colour online.))

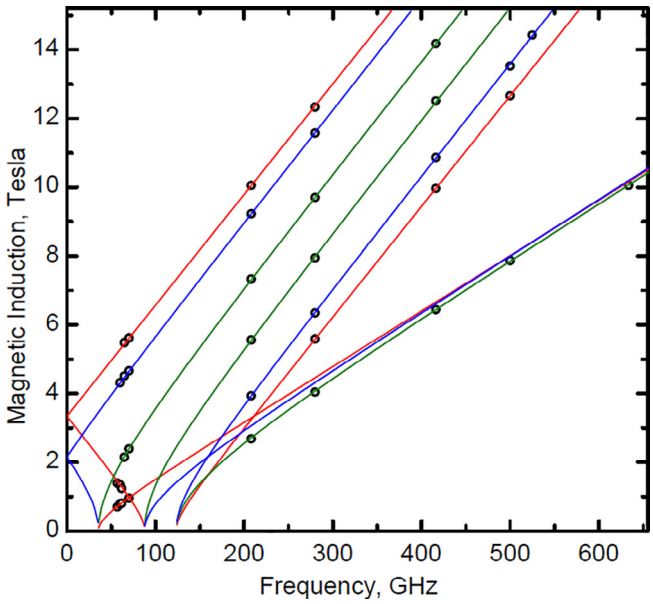

Fig. 14. Frequency dependencies of the EPR transition fields observed for the nickel complex **4**. Circles: experimental points. The green, blue and red solid lines are simulated at the molecular orientations X, Y and Z, respectively. The low-slope traces represent the ΔM_S = 2 (half-field) transitions. ((Colour online.))

The EPR g values in hexacoordinated Ni^{2+} complexes with distorted octahedral environment are related to the ligand-field splitting $^3B_{1g} \rightarrow {}^3B_{2g}$ and $^3B_{1g} \rightarrow {}^3E_g$ (using D_{4h} labeling, see Fig. 9), as are the zero-field splitting parameters D and E: [47]

$$g_{x,y} = g_e - \frac{8\lambda k_{x,y}^2}{E(^3E_g) - E(^3B_{1g})},$$
$$g_z = g_e - \frac{8\lambda k_z^2}{E(^3E_g) - E(^3B_{1g})}, \quad (3)$$
$$D = -2\lambda^2 \left(\frac{2k_z^2}{E(^3E_g) - E(^3B_{1g})} - \frac{2k_{x,y}^2}{E(^3E_g) - E(^3B_{1g})} \right)$$

An approximate relation between the g components and D can be derived

$$D = \lambda(g_z - g_x/2 - g_y/2)/2 \quad (4)$$

The free-ion spin orbit coupling constant λ for Ni^{2+} is reported between −315 cm^{-1} and −336 cm^{-1} [47,48]. With the g components of **4** one gets D between −3.38 cm^{-1}, and −3.61 cm^{-1} in good agreement with the experimental value of −3.508 cm^{-1}. The energies of the $^3B_{1g} \rightarrow {}^3E_g$ and $^3B_{1g} \rightarrow {}^3B_{2g}$ transitions are 8550 cm^{-1} and 9500 cm^{-1} (1180 nm and 1060 nm), respectively (see above) and the orbital reduction factors $k_{x,y}$ and k_z are evaluated to 0.69 and 0.85, respectively.

In the CASSCF [29–31] calculations, which were performed to elucidate the magnitude of the zero-field splitting parameters, the active space consisted of 8 electrons in 5 orbitals, and all 10 triplet and 15 singlet states were taken into account in the calculations of D and E. def2-TZVPP functions were used for all atoms. The initial quasi-restricted orbitals were found in a DFT B3LYP/G calculation. D = −2.93 cm^{-1}, E=−0.94 cm^{-1} (E/D = 0.32, vs experimental 0.17) resulted. The calculated g values were overestimated,

g_x = 2.30, g_y = 2.31 and g_z = 2.33. The contribution of the 3 lowest excited triplet states to the zero-field splitting was overwhelming, while the remaining 7 triplet states contributed 2 orders of magnitude less. Large contributions of 3 excited singlet states were also found, which however almost canceled each other out. When the CASSCF calculation was repeated using only the triplet states, $D = -3.19$ cm^{-1} and E/D = 0.32 were found. The Z axis of the calculated zero-field splitting tensor deviates by 16 deg from the normal to the NiOOOO plane.

3.5.4. HF EPR of the cobalt complex

The cobalt complex **3** exhibited spectra consisting of three features whose effective g values, g_x^{eff} = 5.80, g_y^{eff} = 4.12 and g_z^{eff} = 2.40, (which could be found directly from spectra using $g^{eff} = h\nu/\mu_B B$) were frequency-independent. This is a typical behavior of the high-spin Co(II) complexes with a very large zero-field splitting between the two Kramers doublets M_S=±½ and M_S=±3/2.

The *D* parameter of spin Hamiltonian (**1**) in distorted octahedral high-spin Co(II) may be as large as 100 cm^{-1}. When *D* is sufficiently large and positive, in the HF EPR (as well as in standard X-Band EPR) transitions are observed only within the ground ±½ Kramers doublet, and the spectra may be simulated using an effective S = 1/2 state with g_z^{eff} close to the intrinsic g_z value, while g_x^{eff} and g_x^{eff} are close to doubled intrinsic g_x and g_y. These relations are still modulated by the *E*/*D* ratio. Fig. 15 shows an experimental spectrum of **3** and simulations using either the effective S = 1/2 state with effective g values given above, or using the S = 3/2 state with D = 100 cm^{-1}, E/D = 0.112 and intrinsic $g_x = g_y = g_z$. = 2.5.

The same S = 3/2 simulation will be obtained for any *D* value greater than ~ 50 cm^{-1}, with the g parameters and *E*/*D* ratio as given above, thus the *D* magnitude cannot be determined from HF EPR in this case.

Similarly as it was done for the Ni complex, a calculation of *D* using CASSCF [29–31] was attempted using the X-Ray structure. The active space consisted of 7 electrons in 5 orbitals and 10 quartet states were taken into account in the calculations of *D* and *E*/*D*. Only 4 of these quartet states contributed significantly to *D*. def2-TZVPP functions were used for all atoms. D=+93.7 cm^{-1}, E/D = 0.22, were found. The large positive *D* magnitude is in a qualitative agreement with the EPR spectra.

3.6. In vitro antimicrobial screening

In this study, we examined the antimicrobial properties of compounds **1**–**6**. These compounds contain paratoluic acid (PTA) or 2-bromobenzoic acid (BBA) with metronidazole chelated to the metal ions. Also, Agar well diffusion method was used in this microbiological investigation. A compound that showed inhibition zones above 10 mm is an excellent antimicrobial agent. The zones of inhibition were measured in millimeters and the results are summarized in Table S6. Each of the parent ligands exhibited some antimicrobial activity. Some of the tested compounds exhibited a stronger inhibition effect than the free ligands. A broad antimicrobial spectrum was observed in compounds **1**, **3** and **6**. The rate of killing of the strains observed in these experiments are given accordingly; (i) compound **4** and **6** are comparative in their inhibition against *S. aureus*; (ii) compound **3** and **6** also showed moderate inhibition against *M. luteus* but lower than the strength of the PTA; (iii) against *E. coli*, compound 6 showed the highest killing strength, likewise compound **2** depict moderate action as compared the ligands used; (*iv*) the inhibition zones of the compounds including their ligands showed a very close range in their inhibition strength against *S. typhi*; (v) though compound **6** showed a significant inhibition against *K. pneumonia*, their inhibition zones on the plates are closely related. In summary, Compound **6** showed high antibacterial effect against Gram-positive and Gram-negative bacteria. Compound **2** and **5** are inactive against *M. luteus* and compound **4** is also seen to be inactive against *E. coli*, while compound **6** shows the most significant inhibition against *E. coli* and *K. pneumonia*. It seems that the newly prepared compounds **1**–**6** were most active against Gram-negative (*S. typhi*, *K. pneumonia*) and Gram-positive (*S. aureus*). Also, complex **1** displayed the most active agent against *C. albicans* compared to other complexes. (Supporting Information, Figs. S11, S12).

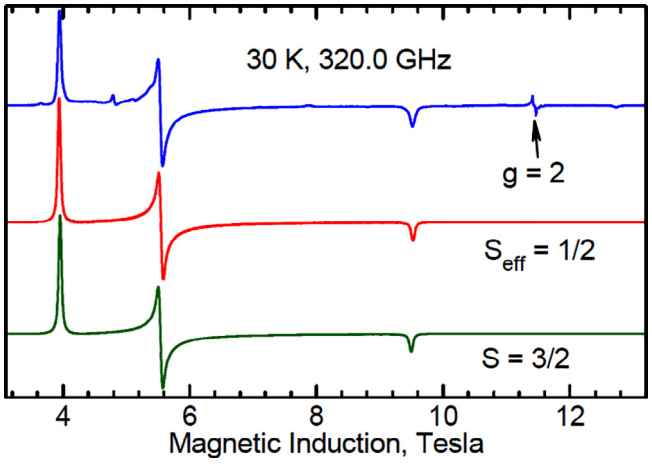

Fig. 15. Top: experimental spectrum of **3.** Middle: simulated using the effective S = 1/2 state. Bottom: simulated using the S = 3/2 state with parameters given in text.

4. Conclusions

In summary, we have synthesized a new binuclear copper(II) complex and five new mononuclear metal(II) complexes bearing benzoic acid derivatives which are supported by metronidazole. The molecular structures of these new compounds were solved by single crystal X-Ray diffraction.

The NIR/Vis/UV diffuse – reflectance electronic spectra of cobalt (II) and nickel(II) complexes were analyzed with the assumption that metal centers adopt pseudo – octahedral elongated (D_{4h}) geometry with *trans* – [$MN_2O_2O'_2$] chromophore. For cobalt(II) complex, the energies of spin – allowed quartet – quartet $^4E_g(1) \rightarrow {}^4B_{2g}$ + $^4E_g(2)$, $^4B_{1g}$, $^4A_{2g}$ and $^4E_g(3)$ transitions are 1150 nm, 615 nm, 495 nm and 470 nm, respectively. For nickel(II) complex, the 1-st and 2-nd *d* – *d* bands are composed of spin – allowed triplet – triplet $^3B_{1g} \rightarrow {}^3E_g(1) + {}^3B_{2g}$ and $^3B_{1g} \rightarrow {}^3E_g(2) + {}^3A_{2g}$ transitions with energies 1180 nm, 1060 nm, 636 nm and 585 nm, respectively. These energies were correlated with the spin Hamiltonian parameters of the nickel complex. Complete Active Space (CASSCF) calculations were attempted to reproduce the zero-field splitting parameters in the Co and Ni complexes resulting in almost quantitative agreement with the experimental data in the Ni case, while large positive D calculated for the cobalt complex was in qualitative agreement with the HF EPR spectra.

CRediT authorship contribution statement

Abiodun A. Ajibola: Conceptualization, Investigation, Methodology, Formal analysis, Writing - original draft. **Joshua A. Obaleye:** Supervision, Conceptualization, Investigation, Writing - review & editing. **Lesław Sieroń:** Investigation. **Waldemar Maniukiewicz:** Software, Investigation, Formal analysis, Writing - review & editing. **Agnieszka Wojciechowska:** Investigation. **Andrew Ozarowski:** Software, Formal analysis, Writing - review & editing.

Declaration of Competing Interest

The authors declare that they have no known competing financial interests or personal relationships that could have appeared to influence the work reported in this paper.

Acknowledgements

The authors gratefully acknowledge the support of the University of Ilorin and Institute of General and Ecological Chemistry, Lodz University of Technology for this research work. The high–field EPR spectra were recorded at the NHMFL, which is funded by the NSF through the Cooperative Agreement No. DMR–1644779 and the State of Florida.

Appendix A. Supplementary data

CCDC 1830902 and 2023694-2023698 contains the supplementary crystallographic data for all compounds. These data can be obtained free of charge via http://www.ccdc.cam.ac.uk/conts/retrieving.html, or from the Cambridge Crystallographic Data Centre, 12 Union Road, Cambridge CB2 1EZ, UK; fax: (+44) 1223-336-033; or e-mail: deposit@ccdc.cam.ac.uk. Supplementary data to this article can be found online at https://doi.org/10.1016/j.poly.2020.114931.

References

[1] X.M. Chen, Y.X. Tong, T.C. Mak, Inorg. Chem. 33 (1994) 4586–4588. P.J. Deuss, K. Barta, Coord. Chem. Rev. 306 (2016) 510–532. Q.X. Wang, Z.L. Yu, Q.H. Wang, W.Q. Li, F. Gao, S.X. Li, Inorg. Chim. Acta 383 (2012) 230–234. S. Saha, S. Jana, S. Gupta, A. Ghosh, H.P. Nayek, Polyhedron 107 (2016) 183–189. J.M. Hao, B.Y. Yu, K. Van Hecke, G.H. Cui, CrystEngComm, 17 (2015) 2279–2293. D.Y. Lee, D.V. Shinde, S.J. Yoon, K.N. Cho, W. Lee, N.K. Shrestha, S.H. Han, J. Phy. Chem. C, 118 (2013) 16328–16334. Q.X. Jia, H. Tian, J.Y. Zhang, E.Q. Gao, Chem. Eur. J. 17 (2011) 1040–1051. J.M. Rueff, N. Masciocchi, P. Rabu, A. Sironi, A. Skoulios, Eur. J. Inorg. Chem. 11 (2001) 2843–2848.

[2] S. Banerjee, S. Shanmugan, R. Murugavel, Struct. Chem. 18 (2007) 165–169. N. Palanisami, R. Murugavel, Inorg. Chim. Acta 365 (2011) 430–438.

[3] (a) R.P. Sharma, A. Saini, D. Monga, P. Venugopalan, J. Jezierska, A. Ozarowski, V. Ferretti, New J. Chem. 38 (2014) 437–447. (b) A. Ozarowski, C. J. Calzado, R. P. Sharma, S. Kumar, J. Jezierska, C. Angeli, F. Spizzo and V. Ferretti. Inorg. Chem. 2015, 54, 11916-11934.

[4] A. Kathiresan, K. Srinivasan, S. Brinda, M. Nethaji, S. Govindarajan, Transition Met. Chem. 37 (2012) 393–397. W.M. Zhang, M.H. Li, J. Sun, P.C. Lv, H.L. Zhu, J. Coord. Chem. 67 (2014) 3519–3531. M. Devereux, M. Curran, M. McCann, M.T. Casey, V. McKee, Polyhedron 15 (1996) 2029–2033. B. Albela, M. Corbella, J. Ribas, I. Castro, J. Sletten, H. Stoeckli-Evans, Inorg. Chem. 37 (1998) 788–798. V. Gómez, M. Corbella, Eur. J. Inorg. Chem. 29 (2009) 4471–4482. R. Sarma, A. Perumal, J.B. Baruah, J. Coord. Chem. 62 (2009) 1513–1524.

[5] U. Kumar, J. Thomas, R. Nagarajan, N. Thirupathi, Inorg. Chim. Acta, 372 (2011) 191–199. M.K. Bhattacharyya, U. Saha, D. Dutta, A. Das, A.K. Verma, A. Frontera. RSC Adv. 9 (2019) 16339–16356. J.-L. Qi, W. Xu, Y.-Q.Z. Zheng, Naturforsch 67b (2012) 1185–1190.

[6] Q. Zhang, L.M. Yu, C.H. Ni, X. Li, X. Li, B. Korean Chem. Soc. 36 (2015) 2190–2197. J. Kavalirova, M. Korabik, P. Stachova, J. Moncol, R. Sillanpaa, T. Lis, D. Miklos, M. Melnık, J. Mrozinski, D. Valigura, Polyhedron 27 (2015) 1333–1342.

[7] Z. Vasková, Z. Padělková, M. Mazur, D. Valigura, J. Moncol, Transition Met. Chem. 36 (2011) 883–889. R.P. Sharma, A. Saini, S. Kumar, J. Kumar, R. Sathishkumar, P. Venugopalan, J. Mol. Struct. 1128 (2017) 135–141. P. Stachová, D. Valigura, M. Koman, M. Melník, M. Korabik, J. Mroziński, T. Glowiak, Polyhedron 23 (2004) 1303–1308.

[8] E.G. Schnitzler, N.A. Seifert, I. Kusuma, W. Jager, J. Phy. Chem. A. 121 (2017) 8625–8631.

[9] V.K. Sandhwar, B. Prasad, Water Conserv. Sci. Eng. 1 (2017) 257–270.

[10] (a) H.L. Zhu, J.L. Qi, J.L. Lin, W. Xu, X.X. Guo, Y.Q. Zheng, Transition Met. Chem. 38 (2013) 733–743. (b) W.D. Song, X.H. Huang, H. Wang, Acta Crystallogr. Sect. 64 (2008) m764–m764. (c) X.K. Yu, X.S. Zhai, Y.Q. Zheng, H.L. Zhu, Zeitschrift für Naturforschung B 69 (2014) 62–70.

[11] G. Evano, N. Blanchard, M. Toumi, Chem. Rev. 108 (2008) 3054–3131.

[12] W. Zhang, G. Pugh, Tetrahedron 59 (2003) 3009–3018.

[13] R.P. Sharma, A. Saini, S. Kumar, P. Venugopalan, V. Ferretti, J. Mol. Struct. 1060 (2014) 256–263. J. Moncol, J. Maroszova, M. Koman, M. Melnik, M. Valko, M. Mazur, T. Lis, J. Coord. Chem. 61 (2008) 3740–3752. J. Halaška, D. Čechová, M. K. Lawson, Z. Růžičková, V. Jorík, M. Koman, M. Valko, B. Kozlevčar, J. Moncol. Chem Papers 70 (2016) 101–113.

[14] A.H. Ceruelos, L.C. Romero-Quezada, J.R. Ledezma, L.L. Contreras, Eur. Rev. Med. Pharmacol. Sci. 23 (2019) 397–401. C.D. Freeman, N.E. Klutman, K.C. Lamp, Drugs 54 (1997) 679–708. A. Bendesky, D. Menéndez, P. Ostrosky-Wegman, Muta. Res.-Rev. Mutat. 511 (2002) 133–144. Samuelson. J. Antimicrob. Agents Chemother. 43 (1999) 1533–1541. S. Demirayak, A.C. Karaburun, N. Kiraz, Eur. J. Med. Chem. 34 (1999) 275–278. S, Löfmark, C. Edlund, C.E. Nord, Clin. Infect. Dis. 50 (2010) S16–S23.

[15] World Health Organization, World Health Organization Model List of Essential Medicines: 21st List 2019. (No. WHO/MVP/EMP/IAU/2019.06). World Health Organization.

[16] N. Galván-Tejada, S. Bernes, S.E. Castillo-Blum, H. Nöth, R. Vicente, N. Barba-Behrens, J. Inorg. Biochem. 91 (2002) 339–348.

[17] A.C. Valderrama-Negrón, W.A. Alves, Á.S. Cruz, S.O. Rogero, D. de Oliveira Silva, Inorg. Chim. Acta, 367 (2011) 85–92. U. Kalinowska-Lis, A. Felczak, L. Chęcińska, K. Zawadzka, E. Patyna, K. Lisowska, J. Ochocki, J. Dalton Trans. 44 (2015) 8178–8189. J.S. Wu, D.G. Shlian, J.H. Palmer, R.K. Upmacis, Acta Cryst. E75 (2019) 1057–1060. F. Athar, K. Husain, M. Abid, S.M. Agarwal, S.J. Coles, M.B. Hursthouse, M.R. Maurya, A. Azam, Chem. Biodivers. 2 (2005) 1320–1330. J.H. Palmer, R.K. Upmacis, Acta Cryst. E71 (2015) 284–287. J.H. Palmer, J.S. Wu, R.K. Upmacis, J. Mol. Struct. 1091 (2015) 177–182. P.J. Quinlivan, J.-S. Wu, R.K. Upmacis, Crystal structure of metronidazolium tetrachloridoaurate (III). Acta Cryst. E71 (2015) 810–812. M. Ratajczak-Sitarz, A. Katrusiak, H. Wojakowska, M. Januszczyk, R. Krzyminiewski, J. Pietrzak. J. Inorg. Chim. Acta 269 (1998) 326–331.

[18] J.A. Obaleye, A.A. Ajibola, V.B. Bernardus, E.C. Hosten, A. Ozarowski, Inorg. Chim. Acta 503 (2020) 119404.

[19] (a) J. Myrczek, Spectrosc. Lett. 23 (1990) 1027–1039. (b) A. Wojciechowska, Z. Staszak, W. Bronowska, A. Pietraszko, M. Cieślak-Golonka, Polyhedron 20 (2001) 2063–2072. (c) A. Wojciechowska, A. Gągor, M. Duczmal, Z. Staszak, A. Ozarowski, Inorg. Chem. 52 (2013) 4360–4371.

[20] O.D. Rigaku, P.R.O. CrysAlis, Rigaku Oxford Diffraction Ltd, Yarnton, Oxfordshire, England, 2019.

[21] G.M. Sheldrick, Acta Cryst. A71 (2015) 3–8.

[22] G.M. Sheldrick, Acta Cryst. C 71 (2015) 3–8.

[23] C.F. Macrae, I.J. Bruno, J.A. Chisholm, P.R. Edgington, P. McCabe, E. Pidcock, L. Rodriguez-Monge, R. Taylor, J. van de Streek, P.A. Wood, J. Appl. Cryst. 41 (2008) 466–470.

[24] (a) J.J. McKinnon, D. Jayatilaka, M.A. Spackman, Chem. Commun. 37 (2007) 3814–3816;
(b) M.A. Spackman, J.J. McKinnon, D. Jayatilaka, CrystEngComm 10 (2008) 377–388;
(c) M.A. Spackman, D. Jayatilaka, CrystEngComm 11 (2009) 19–32;
(d) F.L. Hirshfeld, Theor. Chim. Acta 44 (1977) 129–138;
(e) H.F. Clausen, M.S. Chevallier, M.A. Spackman, B.B. Iversen, New J. Chem. 3 (2010) 193–199.

[25] M.A. Spackmann, J.J. McKinnon, CrystEngComm 4 (2002) 378–392.

[26] S.K. Wolff, D.J. Grimwood, J.J. McKinnon, M.J. Turner, D. Jayatilaka, M.A. Spackman, University of Western Australia, 2012.

[27] L. Noodleman, J. Chem. Phys. 74 (1981) 5737–5743. L. Noodleman, E.R. Davidson, Chem. Phys. 109 (1986) 131–143. L. Noodleman, D. A. Case. Adv. Inorg. Chem. 38 (1992) 423–458. L. Noodleman, D. A. Case. Adv. Inorg. Chem. 38 (1992) 423–458. J.P. Malrieu, R. Caballol, C.J. Calzado, C. de Graaf, N. Guihéry. Chem. Rev. 114 (2014) 429–492. N. Onofrio, J.-M. Mouesca, Inorg. Chem. 50 (2011) 5577–5586. A. Rodríguez-Fortea, P. Alemany, S. Alvarez, E. Ruiz, Inorg. Chem. 41 (2002) 3769–3778.

[28] F. Neese, Surf. Sara: Amsterdam, 2017. F. Neese, Wiley Interdiscip. Rev. Comput. Mol. Sci. 2 (2012) 73–78. A. Schäfer, H. Horn, R. Ahlrichs, J. Chem. Phys. 97 (1992) 2571–2577. R. Ahlrichs, et al., unpublished. The Ahlrichs auxiliary basis sets (https://www.1326 basissetexchange.org/) have been hardwired into the ORCA software. K. Eichkorn, O. Treutler, H. Öhm, M. Häser, R. Ahlrichs, Chem. Phys. Lett. 240 (1995) 283–290. K. Eichkorn, F. Weigend, O. Treutler, R. Ahlrichs, Theor. Chem. Accounts Theory, Comput. Model. (Theoretica Chim. Acta) 97 (1997) 119–124. A.D. Becke, Phys. Rev. A 38 (1988) 3098–3100. J.P. Perdew, Phys. Rev. B 33 (1986) 8822–8824. J.P. Perdew, Phys. Rev. B 34 (1986) 7406–7406. R.A. Kendall, H.A. Früchtl, Theor. Chem. Accounts Theory, Comput. Model. (Theoretica Chim. Acta) 97 (1997) 158–163.

[29] B.O. Roos, P.R. Taylor, P.E.M. Sigbahn, Chem. Phys. 48 (1980) 157–173.

[30] C. Angeli, R. Cimiraglia, S. Evangelisti, T. Leininger, J.-P. Marlieu, J. Chem. Phys. 114 (2001) 10252–10264.

[31] F. Neese, J. Chem. Phys. 127 (2007) 164112.

[32] (a) M.I. Choudhary, W.J. Thomsen, CRC Press, 2001. (b) A.W. Bauer, W.M.M. Kirby, J.C. Sherris, M. Turck, Am. J. Clin. Pathol. 45 (1966) 493-496.

[33] M. Melnik, Coord. Chem. Rev. 36 (1981) 1–44.

[34] F. Sánchez-Férez, M. Guerrero, J.A. Ayllón, T. Calvet, M. Font-Bardia, J.G. Planas, J. Pons, Inorg. Chim. Acta 487 (2019) 295–306. D.B. Dell'Amico, A. Di Giacomo, L. Falchi, L. Labella, M. Marelli, C. Evangelisti, M. Lezzerini, F. Marchetti, S. Samaritani, Polyhedron 123 (2017) 33–38.

[35] A.W. Addison, T.N. Rao, J. Reedijk, J. van Rijn, G.C. Verschoor, J. Chem. Soc., Dalton Trans. 7 (1984) 1349–1356.

[36] M. Guerrero, J.A. Ayllón, T. Calvet, M. Font-Bardia, J. Pons, Polyhedron 134 (2017) 107–113. P. Mosae Selvakumar, S. Nadella, J. Sahoo, E. Suresh, P.S. Subramanian, J. Coord. Chem. 66 (2013) 287–299. J. Hermle, G. Meyer, Acta Cryst. E67 (2011) m1089. A.G. Bellesis, C.P. Landee, M. Polson, M.M. Turnbull, J. L. Wikaira, Eur. Chem. Bull. 4 (2015) 110–116. M. Barquín, M.J. González Garmendia, L. Larrínaga, E. Pinilla, J. M. Seco, M.R. Torres, J. Coord. Chem. 63 (2010) 1652–1665. S. Youngme, A. Cheansirisomboon, C. Danvirutai, C.

Pakawatchai, N. Chaichit, C. Engkagul, G.A. van Albada, J.S. Costa, J. Reedijk, Polyhedron 27 (2008) 1875–1882. P. Segl'a, V. Kuchtanin, M. Tatarko, J. Svorec, J. Moncol, M. Valko. Chem. Pap. 72 (2018) 863–876. T. Kawata, H. Uekusa, T. Furukawa, T. Tokii, Y. Muto, M. Kato, S. Ohba, Acta Crystallogr. Sect. B48 (1992) 253–261.
[37] A.B.P. Lever, New York, Elsevier, 1984.
[38] (a) H. Manaa, Y. Guyot, R. Moncorge, Phys. Rev. B 48 (1993) 3633–3645. (b) T. Titis, J. Hudak, J. Kozisek, A. Krutosikova, J. Moncol, D. Tarabova, R. Boča, Inorg. Chim. Acta 388 (2012) 106–113.
[39] J.L. Pascual, Phys. Rev. B 67 (2003) 115112.
[40] J. Titis, R. Boča, Inorg. Chem. 50 (2011) 11838–11845. (b) H. Souissi, S. Kammoun, Mater. Sci. Appl. 2 (2011) 1121–1126. (c) M. Wildner, J. Solid. State Chem. 115 (1995) 360–367. (d) M. Wildner, Phys. Chem. Miner. 23 (1996) 489–496. (e) S. Chandra, D. Jain, A.K. Sharma, P. Sharma, Molecules 14 (2009) 174–190. (f) M. Puszyńska-Tuszkanow, M. Daszkiewicz, G. Maciejewska, A. Adach, M. Cieślak-Golonka, Struct. Chem. 21 (2010) 315–321. (g) P. Diaz-Gallifa, O. Fabelo, J. Pasan, L. Candillas-Delgado, F. Lloret, M. Julve, C. Ruiz-Perez, Inorg. Chem. 53 (2014) 6299–6308.
[41] (a) L.Y. Martin, C.R. Sperati, D.H. Busch, J. Am. Chem. Soc. 99 (1977) 2968–2981. (b) J.C. Donini, B.R. Hollebone, G. London, A.B.P. Lever, J.C. Hempel, Inorg. Chem. 14 (1975) 455–461. (c) J.R. Perumareddi, J. Phys. Chem. 76 (1972) 3401–3411. d) A. Wojciechowska, M. Daszkiewicz, Z. Staszak, A. Trusz-Zdybek, A. Bienko, A. Ozarowski, Inorg. Chem. 50 (2011) 1132–11542.
[42] M. Puszyńska-Tuszkanow, M. Daszkiewicz, G. Maciejewska, Z. Staszak, J. Wietrzyk, B. Filip, M. Cieślak-Golonka, Polyhedron 30 (2011) 2016–2025.
[43] J. Miklovič, A. Packová, P. Segl'a, J. Titiš, M. Koman, R. Boča, V. Jorík, H. Krekuska, D. Valigura, Inorg. Chem. Acta 429 (2015) 73–80.
[44] A. Ozarowski, Inorg. Chem. 47 (2008) 9760–9762. A. Ozarowski, I.B. Szymanska, T. Muziol, J. Jezierska, J. Am. Chem. Soc. 131 (2009) 10279–10292.
[45] R. Maurice, K. Sivalingam, D. Ganyushin, N. Guihery, C. de Graaf, F. Neese, Inorg. Chem. 50 (2011) 6229–6236.
[46] D.L. Reger, A. Debreczeni, M.D. Smith, J. Jezierska, A. Ozarowski, Inorg. Chem. 51 (2012) 1068–1083.
[47] R. Boča, Struct. Bond. 117 (2006) 1–264. R. Boča, Coord Chem. Rev. 248 (2004) 757–815.
[48] J. Bendix, M. Brorson, C.E. Schaeffer, Inorg. Chem. 32 (1993) 2838–2849.